Design for Integrated Planar Spiral Inductor for MEMS

Yamina Benhadda, Mokhtaria Derkaoui, Kheira Mendaz, Hayet Kharbouch, Pierre Spitéri

https://doi.org/10.3311/PPee.21666

Periodica Polytechnica Electrical Engineering and Computer Science

Design for Integrated Planar Spiral Inductor for MEMS

Yamina Benhadda[1*], Mokhtaria Derkaoui[2], Kheira Mendaz[3], Hayet Kharbouch[1], Pierre Spiteri[4]

[1] LEPA Laboratory, Department of Electrical Engineering, Faculty of Electrotechnics, University of Science and Technology of Oran Mohamed-Boudiaf, 31000 Oran, P.O.B. 1505, Algeria
[2] LEPA Laboratory, National Institute of Telecommunications & ICT of Oran, 31000 Oran, P.O.B. 1518, Algeria
[3] Department of Electrical Engineering, University Belhadj Bouchaib Ain Temouchent, N101 Route de Sidi Bel Abess, 46000 Ain Temouchent, Algeria
[4] Institute de Recherche en Informatique de Toulouse (IRIT), L'École Nationale Supérieure d'Électrotechnique, d'Électronique, d'Informatique, d'Hydraulique et des Télécommunications (INP-ENSEEIHT), 31071 Toulouse, P.O.B. 7122, France
* Corresponding author, e-mail: yamina.benhadda@univ-usto.dz

Received: 08 December 2022, Accepted: 05 May 2023, Published online: 21 June 2023

Abstract

The main aim of this paper is to present the new design of an integrated planar spiral inductor with a new structure of an underpass to obtain a high inductance, high quality factor and minimum losses into winding and magnetic core. The performance of this structure dependent on the geometrical, electrical parameters and material properties. These parameters are calculated at 350 MHz and this is the high frequency used for MEMS applications. Furthermore, thermal analysis in inductor from finite difference method is described. The heat transfer model is based on heat conduction and heat convection. Moreover, the heat source is calculated by different losses. In addition, the simulation results from 3D finite element method using software also been presented in this paper. It is based on both the classical heat equation and certain condition limits. However, a new design of an underpass has been proposed where a via is fabricated with a circular layer. The input and output of the spiral are implanted in the same direction. In addition, the magnetic core is the solution to decrease the temperature. Finally, the results of the finite difference method are compared with simulation results from finite element method. The good agreement between the results is obtained. The proposed via and a core magnetic are responsible for enhancement the thermal behavior in integrated inductor. The result shows that the temperature of the air core inductor and magnetic core inductor could be 53 °C and 33 °C, respectively.

Keywords

integrated planar spiral inductor, underpass, finite difference method, 3D finite element method, temperature

1 Introduction

Inductors are an important part of switching power converters. These components store electrical energy [1, 2]. When an inductor is operated in switching power converters, an increased power loss in the assembly is observed due to the effect of the current flowing through the inductor windings on the magnetic reversal of its core [3]. Losses in the inductor are converted to heat. Due to self-heating phenomena and mutual thermal coupling between the inductor core and windings, the heat generated in the inductor assembly causes the temperature of the core and windings to rise above the ambient temperature [4].

Thermal modeling and simulation has become an important part of process design. These integrated components are magnetic in nature. Modeling these components provides an excellent study to determine the temperature evolution. Temperature greatly affects the characteristics of electronic components, especially their reliability. Therefore, it is important to know the temperature value of each component under the expected operating conditions [5].

Given this mentioned importance, many researchers have submitted analytical and simulations work related to thermal behavior in integrated inductor. Among the first researchers to have carried out this type of work, Allaoui et al. [6] who introduced an analytical work and numerical simulations in integrated inductor with classical underpass. Coulibaly et al. [7] proposed compact thermal model that can be integrated into mathematical tools to achieve temperature distribution across the integrated LC component. Calculation of temperature distribution is based on the assumption that the temperature line is linear under steady state. Detka and Górecki [8] carried out a study, nonlinear thermal model of the inductor takes

Cite this article as: Benhadda, Y., Derkaoui, M., Mendaz, K., Kharbouch, H., Spiteri, P. "Design for Integrated Planar Spiral Inductor for MEMS", Periodica Polytechnica Electrical Engineering and Computer Science, 2023. https://doi.org/10.3311/PPee.21666

into account the fact that both the core temperature and the winding temperature depend on the value of ambient temperature and a temperature excess. Derkaoui et al. [9] studied by numerical voice, the thermal behavior in an octagonal inductor with a classical underpass.

The purpose of this research will be a contribution to the study of the thermal effect in a new design of integrated planar spiral inductor contain underpass with circular via. Furthermore, the maximum temperature rise of the proposed inductor is 33 °C. In other words, the inductor can due to too high temperature 80 °C.

There are several methods to increase the temperature inside inductor. In the aspect of the topology, adding the number of turns of the winding is straightforward for a spiral structure. However, the high inductance value could downgrade the efficiency of inductor. Also, the proximity effect caused by the multi-turn spiral would further decrease the efficiency as the high frequency. In addition, the total length of winding in traditional planar inductor required by the complicated topology and the interface of the via in an underpass are responsible for increasing temperature value. Under this circumstance, the via in an underpass and a magnetic core inductor would be a solution to lowering the thermal resistance and miniaturization.

Our aim is to use a simple structure of an underpass including circular via to suppress temperature and improve the inductance by adding the magnetic core. This magnetic core is fabricated with ferrite, enabling its good compatibility with the semiconductor process used in industry.

2 Concept and design of integrated inductor

Integrated inductors are used in everything from blood pressure sensors to electronic money cards. These coils are located on a printed circuit board and are a good choice for inductive coupling, especially if space is limited. They take up less space than other inductors and are therefore suitable for any application with size constraints such as MEMS or implanted medical devices such as heart pumps. These inductors can be fabricated on rigid and non-rigid surfaces, which means they can be integrated onto printed circuit boards (PCBs) and flex circuits efficient manufacturing process. Due to these properties, integrated planar spiral inductors have many different use cases, mainly in the high frequency range. Some examples include, remote health monitoring (e.g., blood pressure sensors), wireless power transfer (e.g., wearable/implantable medical devices), RF identification (e.g., e-money cards) and induction heating (e.g., induction cooktops). In the low frequency, these inductors are used by amateur radio operators. Other areas are military applications like submarines, RFID tags in near-field communication, and some low-frequency radio broadcasting.

The integrated planar spiral inductor can be characterized by the following design parameters, the number of turns n, the width of the conductor w, thickness of the conductor t, the spacing between conductor s, length of the conductor l, the outer diameter d_{out}. Fig. 1 shows the geometry of the inductor corresponding to the design parameters.

The 3D view of air core inductor topography considered in this work is shown in Fig. 2 where the underpass including a via fabricated with a circular Cu layer. Also, the input and output of a spiral are implanted in the same direction.

Fig. 3 shows a physical model of a magnetic core integrated. The copper (Cu) is used as the conductor winding. The silicon dioxide (SiO_2) is used as the dielectric layer. This material consists of 25 μm thick. The ferrite (NiFe) is used as the substrate layer. This material consists of 25 μm thick and it is widely used for the device fabrication and as the substrates of MEMS sensors. The resistivity of the ferrite produces a low eddy current in the substrate enhancement the inductance and quality factor.

Many different structures have been proposed for integrated inductors [10, 11] but the most successful is shown in Fig. 4.

The inductance L and the resistance R_s represent the inductance and resistance of the spiral and underpass respectively. The overlap between the spiral and the underpass allows capacitive coupling between the two terminals of the inductor C_s. C_{ox} models the dioxide capacitance between the spiral and the substrate. The capacitance and resistance of the substrate are modeled by the C_{sub} and R_{sub}.

Table 1 contains the specifications and the design results of the integrated planar spiral inductor.

The design results of integrated inductor are shown in Table 1, including the inductance, output diameter, number of turns, thickness of the conductor, width of the conductor, and spacing between conductor.

The electrical parameters values of the model parameters for the integrated inductor are listed in Table 2.

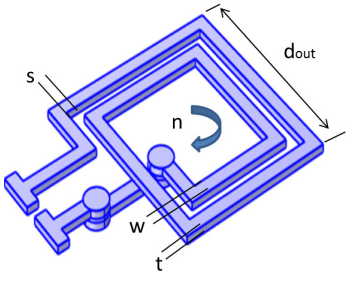

Fig. 1 Geometry of integrated planar spiral inductor

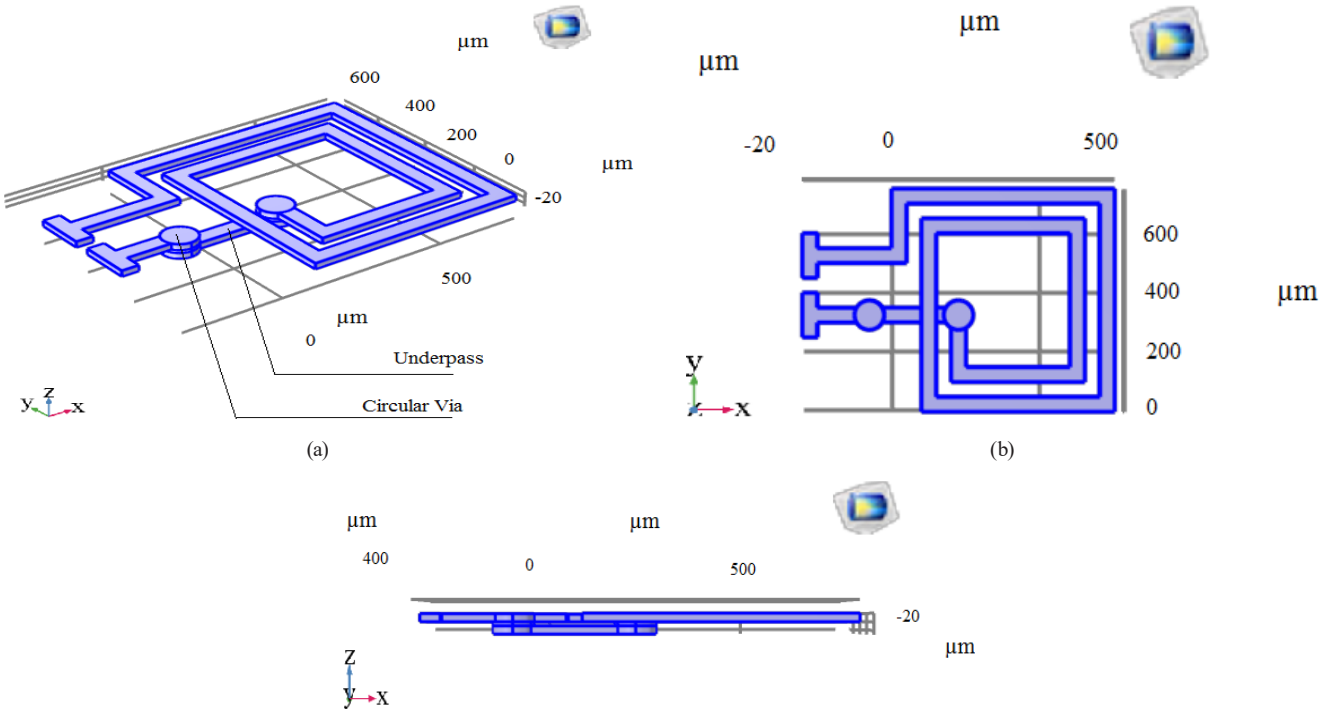

Fig. 2 Air core integrated inductor topography, (a) general view, (b) top view, (c) front view

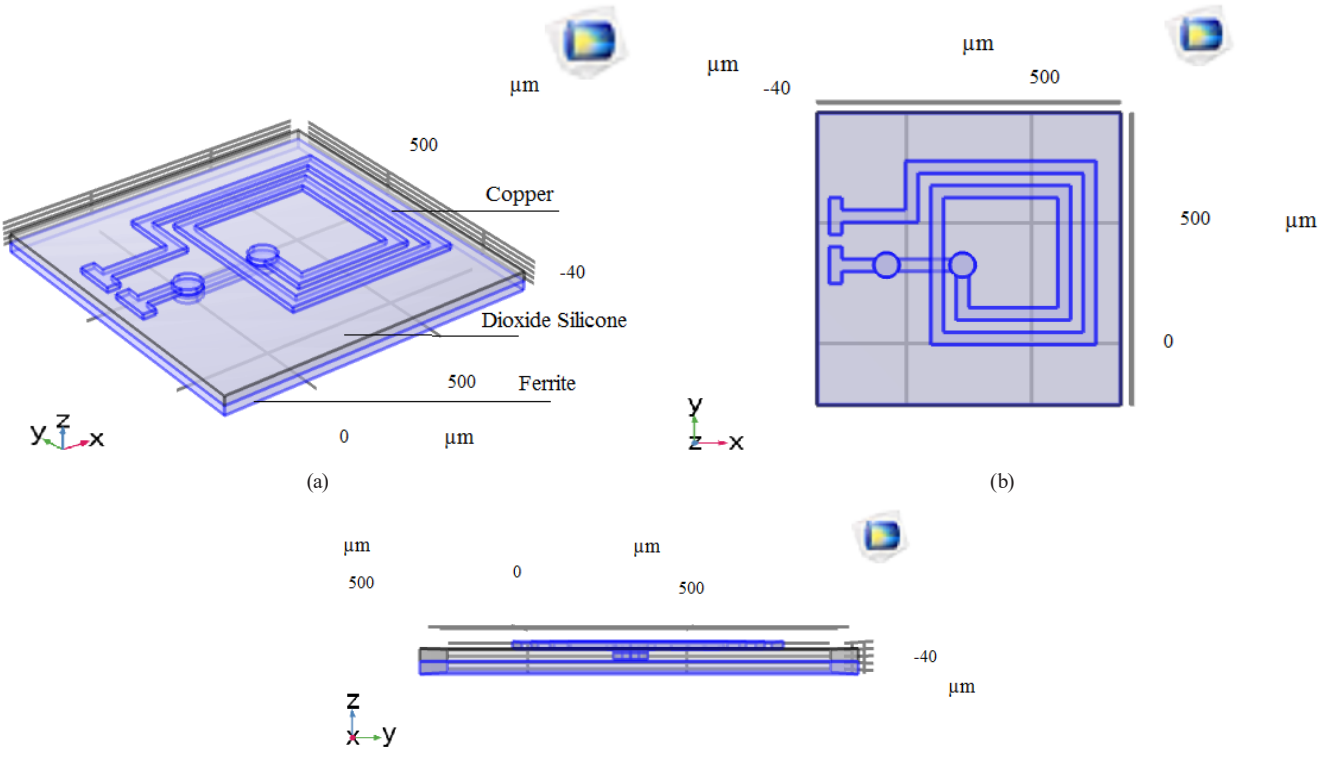

Fig. 3 Magnetic core integrated inductor topography, (a) general view, (b) top view, (c) front view

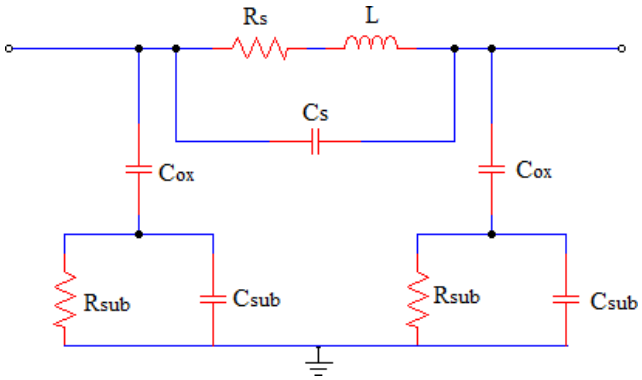

Fig. 4 Equivalent circuit of an integrated inductor

Table 1 Design results of the integrated inductor

Parameter	Value
Inductance, L (H)	1.13×10^{-6}
Output diameter, d_{out} (m)	750×10^{-6}
Number of turns, n	2
Thickness of the conductor, t (m)	20×10^{-6}
Width of the conductor, w (m)	10×10^{-6}
Spacing between conductor, s (m)	10×10^{-6}

Table 2 Extracted values of the model parameters for the integrated inductor

Electricals parameters	Values
R_s (Ω)	0.0515
R_{sub} (Ω)	0.0032
C_s (F)	2.9808×10^{-14}
C_{ox} (F)	1.5694×10^{-7}
C_{sub} (F)	5.1363×10^{-13}

The performance parameters of the integrated inductor are calculated from the Z-parameters extracted from S-parameters [12, 13].

$$Z_{11} = Z_0 \frac{(1+S_{11})\times(1-S_{22})+S_{12}^2}{(1-S_{11})\times(1-S_{22})-S_{12}^2}$$
$$Z_{21} = Z_{12} = Z_0 \frac{2\times S_{12}}{(1-S_{11})\times(1-S_{22})-S_{12}^2} \quad (1)$$
$$Z_{22} = Z_0 \frac{(1+S_{11})\times(1-S_{22})+S_{12}^2}{(1-S_{11})\times(1-S_{22})-S_{12}^2}$$

The expression used to extract a quality factor Q of the inductor in a 2-port configuration is represented by Eq. (2). Other important parameters extracted from the inductor are the inductance L calculated by Eq. (3), and resistance (R) computed by Eq. (4).

$$Q = \frac{\mathrm{Im}(Z_{11})}{\mathrm{Re}(Z_{11})} \quad (2)$$

$$L = \frac{\mathrm{Im}(Z_{11})}{f} \quad (3)$$

$$R = \mathrm{Re}(Z_{11}) \quad (4)$$

Fig. 5 shows the evolution of the quality factor as a function of frequency for the inductor. At low frequency, the quality factor is presented by $L \times \omega/R_s$ represents the magnetic energy stored and the ohmic losses in the series resistance R_s. It is associated to the ideal behavior of the component. The rapid degradation of the quality factor at high frequency is related to the combined effect of the dielectric and substrate losses. The self-resonant frequency (SRF) is caused by the parasitic capacitances and offers an estimation of the maximum operating frequency of the component.

Fig. 6 shows the evolution of the inductance as a function of frequency for the inductor. At low frequencies, the influence of parasitic capacitance is small, the inductance value remains relatively constant, and the inductance can be used as an inductive element. The transition region where the reactance value becomes negative and crosses zero, which is the self-resonance frequency when the peak electric and magnetic energies are equal. Therefore, the inductance tends to zero at the self-resonant frequency. At high frequencies, integrated inductor exhibits capacitive behavior, and a quality factor has a negative value.

Fig. 7 shows the evolution of the resistance as a function of frequency for the inductor. At low frequencies the quality factor rises with frequency, because the losses are relatively constant mainly due to the resistance R_s of the metal lines, while the imaginary part of the impedance is

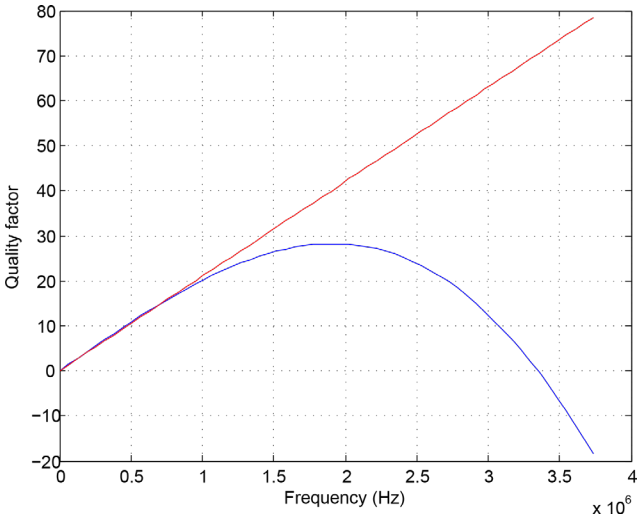

Fig. 5 Quality factor versus frequency

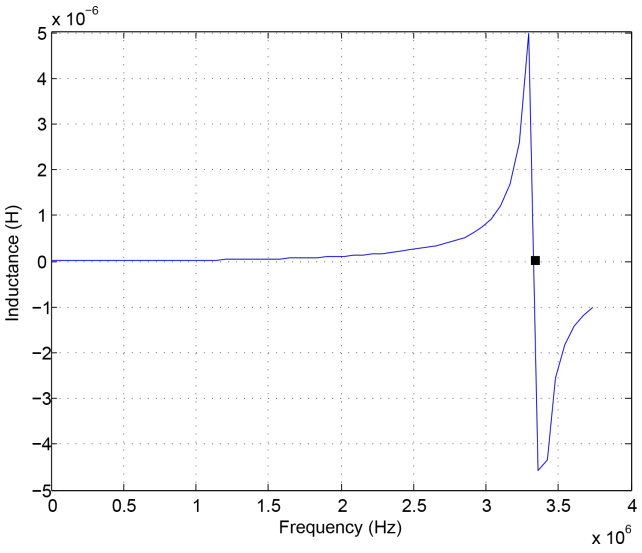

Fig. 6 Inductance versus frequency

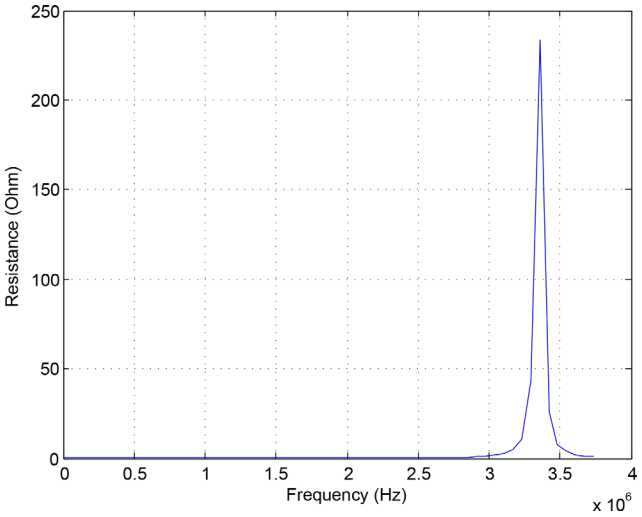

Fig. 7 Resistance versus frequency

increasing to flow through the parasitic capacitance of the substrate, causing energy loss and increasing the effective resistance. In addition, the skin effect begins to raise the resistance of metal at higher frequencies.

Fig. 8 shows the evolution of impedance for the inductor. If the frequency increase, the impedance becomes substantial. At a certain frequency, it will be equal to the impedance of the component. Consequently, the inductor will begin to resonate. The imaginary part of the impedance will be equal to zero [14].

Fig. 9 shows the evolution of the phase. At low frequencies the phase for inductor is in the range of 80° ~ 90°. At the self-resonant frequency, the inductor resonates, and at high frequencies, the phase have a negative value.

Fig. 10 shows the simulated S-parameters results of the integrated inductor based on Z impedance. The insertion losses could be the most important characteristic to

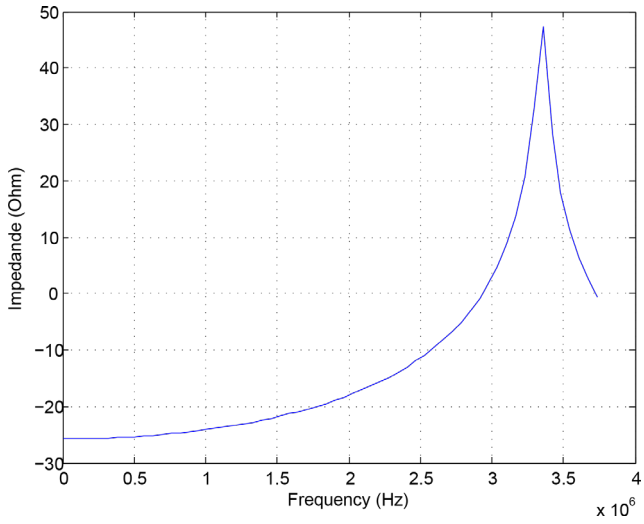

Fig. 8 Impedance versus frequency

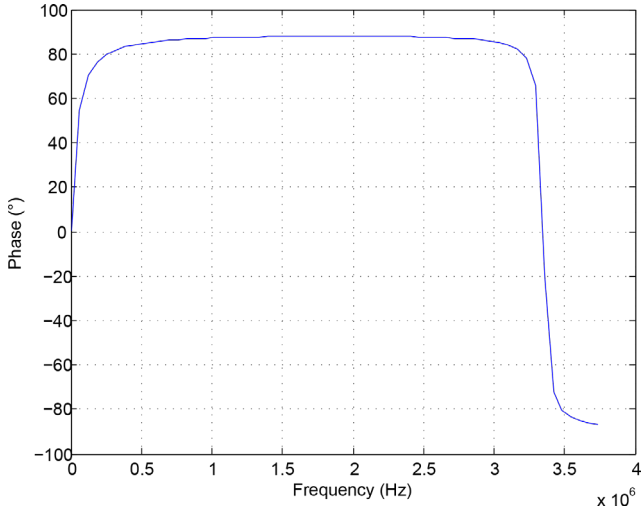

Fig. 9 Phase versus frequency

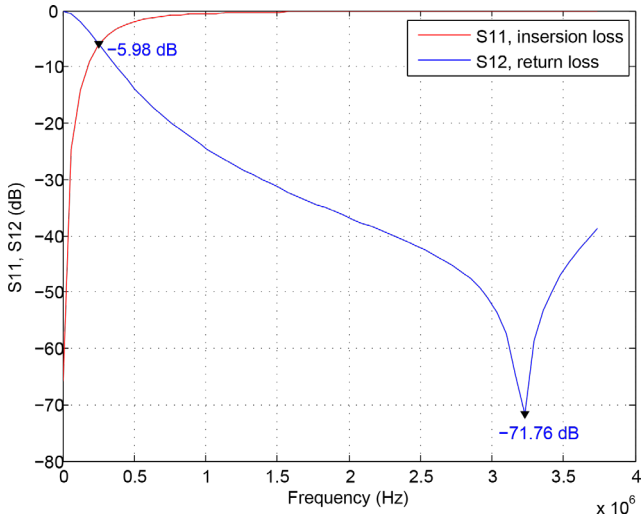

Fig. 10 Insertion and return losses versus frequency

evaluate the performance of integrated inductor since they give an idea of an efficiently. Insertion losses are

determined by metal ohmic losses and substrate dissipation. This inductor offers high performances in terms of size, insertion loss plus return loss.

Fig. 11 shows Smith chart plot of S-parameters obtained from the electrical equivalent circuit using the design for the integrated inductor.

3 Thermal modeling of the integrated inductor

Section 3 concerns a description of the temperature inside a planar integrated inductor, using 1D finite difference method analytical calculation and 3D finite element method simulation [15–17]. Equation (5), which describes the thermal model, can be expressed as follows:

$$\rho \times C_p \frac{\partial T}{\partial t} - \nabla\left(k \nabla T\right) = q. \tag{5}$$

The heat source is given by:

$$q = \frac{P}{V}, \tag{6}$$

$$P = P_{Winding} + P_f + P_{ed}, \tag{7}$$

where:

- P: losses in inductor;
- V: Volume of inductor.

For electronics devices research, reducing losses is key output. Losses in planar integrated inductors include copper losses and core loss. There are many effective ways to reduce core loss, including choosing better core materials and eliminating magnetic flux. There are many ways to reduce copper loss, Joule losses in the winding. However, research on skin effect and proximity effect has mainly focused on conductors and round conductor windings [18–28].

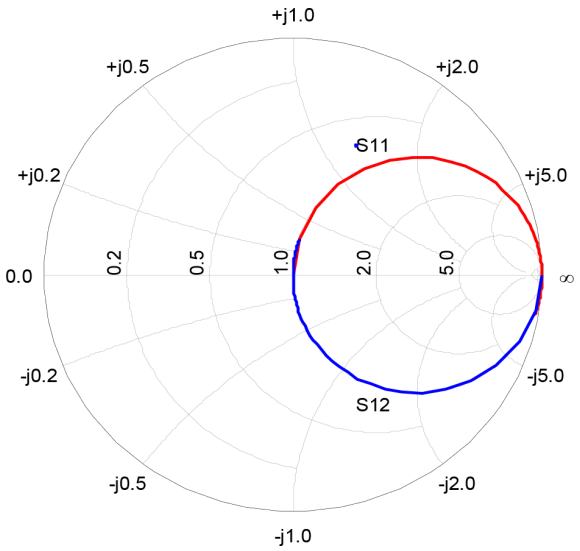

Fig. 11 Smith chart plot of S-parameters

Joule losses also known Joule heating. It is generated by the current flowing through the winding conductors. As frequency increases, skin and proximity effects increase the resistance of the windings, which increases losses.

Joule losses in the winding are calculated by the expressions:

$$P_{Winding} = R_s I_{savg}^2 + R_{AC} I_L^2. \tag{8}$$

Every time the magnetic field reverses, a small amount of energy is lost due to hysteresis losses in the core.

The Hysteresis losses in the core are given by this formula:

$$P_f = m f^{\alpha} B_{\max}^{\beta} V, \tag{9}$$

where m, α and β are the coefficients depend on the size of the material.

Eddy current losses, also known as Foucault currents. Ferromagnetic materials are also good conductors, and a core made of this material will also be shorted with a single turn over its entire length. Eddy currents thus circulate within the core in a plane perpendicular to the magnetic flux and cause resistive heating of the core material.

The Eddy current losses are defined as follows:

$$P_{ed} = C \frac{f^2 B^2}{\rho}, \tag{10}$$

where C and ρ are the coefficients depend on the size of the material.

In Fig. 12, which illustrates how electrical potential distributes in the air core inductor at 350 MHz by COMSOL Multiphysics 3D simulation [29], there is a severe electrical potential concentration on the input conductor near the underpass and a via.

The magnetic flux density concentrates at the inner corner of air core inductor, shown in Fig. 13, leading to more magnetic losses.

Loss density distributes in the air core inductor is displayed in Fig. 14. The loss is pushed to the inner side of turns of the conductor. This is due to the proximity effect, which takes place when a conductor is under the influence of a time-varying field. In the inductors, the skin-effect eddy current and the proximity-effect eddy current superimpose to form the total eddy current distribution, resulting in the increase of the resistance.

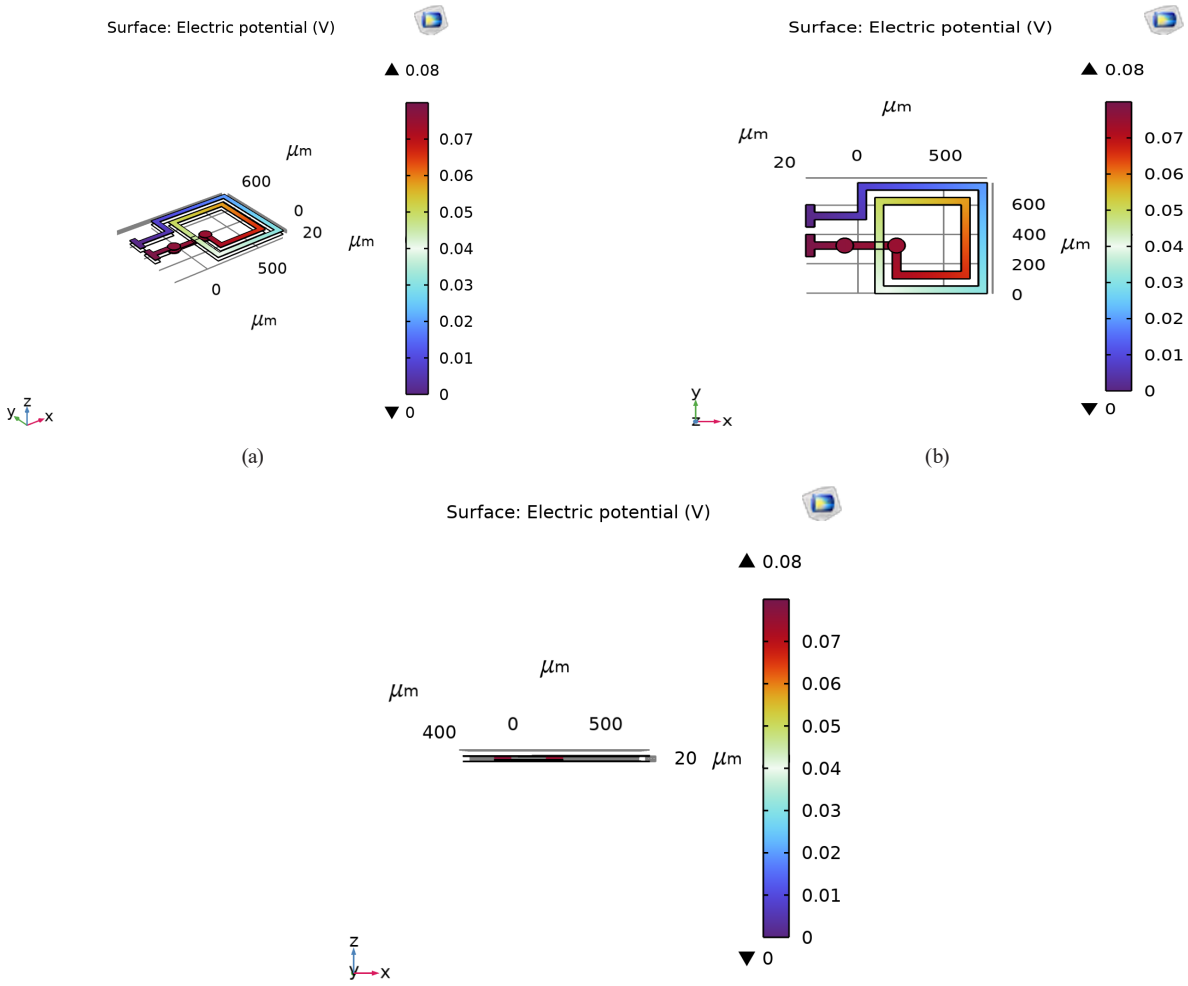

Fig. 12 Electrical potential distributes in the air core inductor, (a) general view, (b) top view, (c) front view

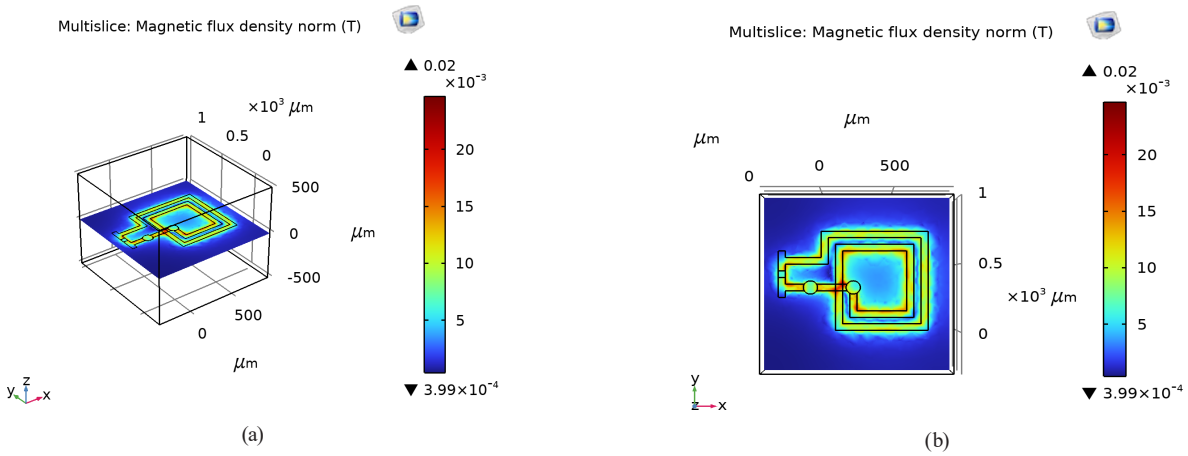

Fig. 13 Magnetic flux density distributes in the air core inductor, (a) general view, (b) top view

3.1 Finite difference method analytical calculation

For the numerical solution of the heat equation, a discretization by the finite difference method and an implicit time is defined:

$$\left(1+\alpha \boldsymbol{B}_i\right)T_i^{n+1} = dt \times F_i^{n+1} + T_i^n, \tag{11}$$

where:

- $\boldsymbol{B}_i$: discretization matrix,
- n: index of time, $t_n = n\ dt$,
- dt: time step,
- Δx and Δy: discretization steps in the axis X and Y.

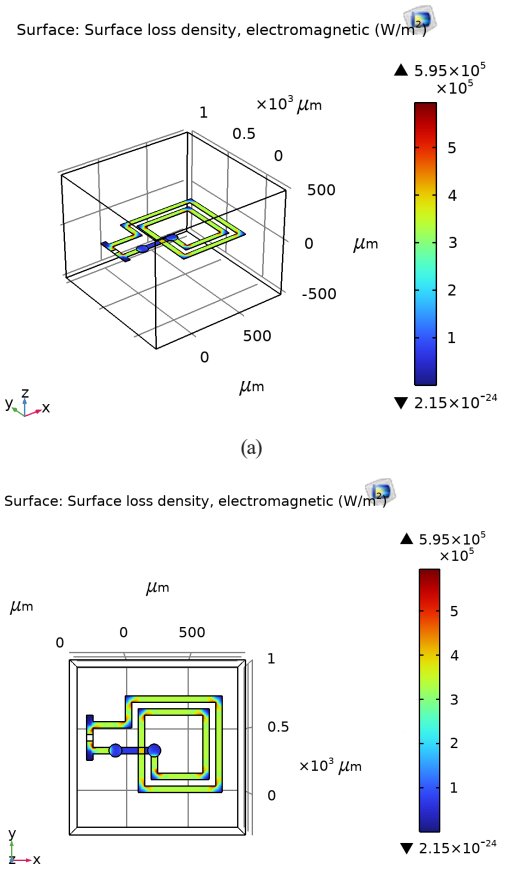

Fig. 14 Loss density distributes in the air core inductor, (a) general view, (b) top view

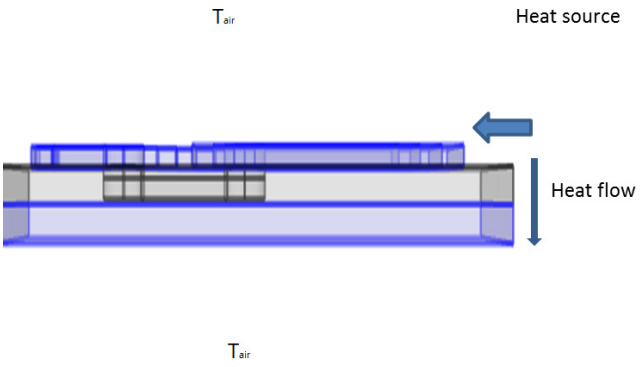

Fig. 15 Cross section of the integrated inductor showing heat flow from heat source

At $t = t_{n+1} = (n+1)dt$, the numerical scheme is given by:

$$T_M^{n+1} - T_M^n - \alpha_x dt\left(T_W^{n+1} - 2T_M^{n+1} + T_E^{n+1}\right) - \alpha_y dt\left(T_N^{n+1} - 2T_M^{n+1} + T_S^{n+1}\right) = dtF_M^{n+1} + T_M^n, \tag{12}$$

$$\alpha_{ix} = \frac{\lambda_i dt}{C_i \rho_i \Delta x\ \Delta x}, \tag{13}$$

$$\alpha_{iy} = \frac{\lambda_i dt}{C_i \rho_i \Delta y\ \Delta y}, \tag{14}$$

where:

- F_M^{n+1} : heat source,
- C_i: specific heat of the material i,
- ρ_i: volume mass of the material i.

Fig. 15 shows a cross section of the integrated planar spiral inductor showing heat flow from a heat source.

The temperature difference between inside and outside is composed of heat conduction and heat convection. The heat loss rate is given by Eq. (15):

$$Q = \frac{\lambda A\left(T_1 - T_2\right)}{d}, \tag{15}$$

where:

- Q: heat flow (W),
- T_1, T_2: temperatures at the ends of the solid material (°C),
- d: thickness crossed by the heat source (m),
- A: surface of a solid material (m^2),
- λ: thermal conductivity of the material (W/(m K)).

On the outer surface of a solid material, heat transfer is mainly heat convection between the air and the surface. It calculates according to Newton's law of cooling:

$$Q = h \times A \times \left(T_f - T_a\right), \tag{16}$$

where:

- Q: rate of heat flow (W),
- h: convective heat transfer coefficient (W/m^{2}K),
- A: cross sectional area (m^2),
- T_f: surface temperature (°C),
- T_a: ambient temperature (°C).

To simplify the modeling of the inductor, some assumptions are made:

- each layer must satisfy the heat conduction equation,
- one-dimensional heat flow,
- constant material properties,
- uniform heat flow in each layer,

Table 3 Thermals properties of the materials

Materials	Conductor Copper (Cu)	Substrate Ferrite (NiFe)	Dielectric Silicon Dioxide (SiO_2)
Thermal conductivity: k (W/m K)	400	30	1.4
Heat capacity: C_p (J/K kg)	385	700	350
Density: r_{h0} (kg/m^3)	1	4000	200

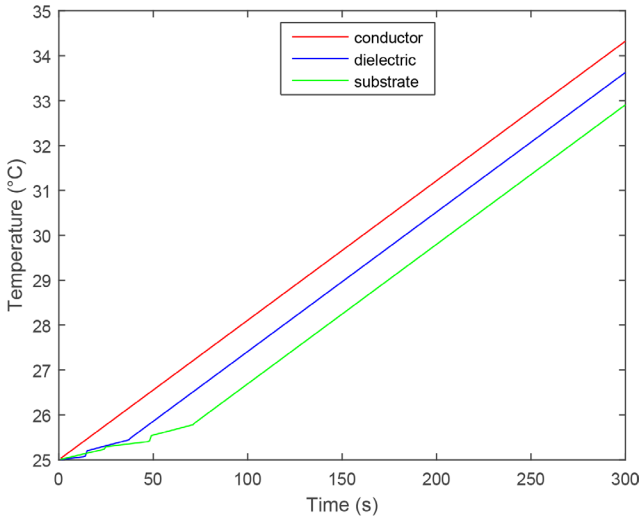

Fig. 16 Variation of temperature versus time in the different layers

- perfect contact between layers with uniform thickness,
- temperature inside the spiral can be considered uniform,
- in faces, ambient temperature (T_a) near the top and bottom,
- in faces, the convective heat transfer coefficient $h = 10$ W/m^2/K representing natural convection,
- the flow is fixed on each upper face is given by: generated heat source Q inside the component,
- the flux is fixed on each upper face and is given by:

$$\lambda_i \frac{dT_i}{dy} = \varphi_i, \tag{17}$$

- the continuity condition at the interface is given by:

$$\lambda_i \frac{dT_i}{dy} = \lambda_{i+1} \frac{dT_{i+1}}{dy}, \tag{18}$$

- the initial temperature is given by:

$$T(x, y) = T_a. \tag{19}$$

Table 3 gives the property values of the materials used for thermal modeling and simulation of the inductor. Such a model should include substrate t_{sub} = 20 µm, dielectric t_{ox} = 20 µm and metal layers t = 20 µm. Each material that makes up these objects is described using properties such as thermal conductivity, heat capacity, and density.

Fig. 16 shows the temperature variation over time of the various layers of the component.

The temperature distribution calculated analytically by the component for each physical case of the heat transfer coefficient according to the finite difference method is shown in Fig. 17 (a)–(c).

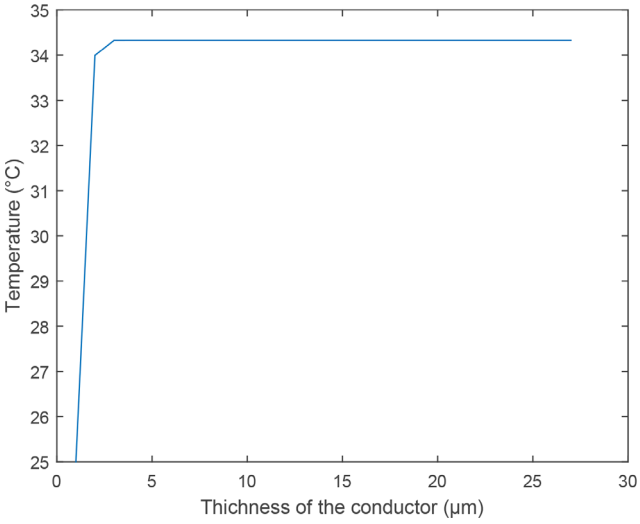

(a)

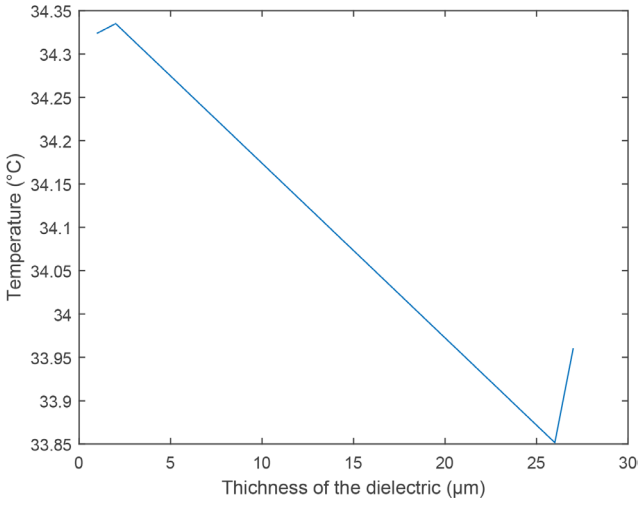

(b)

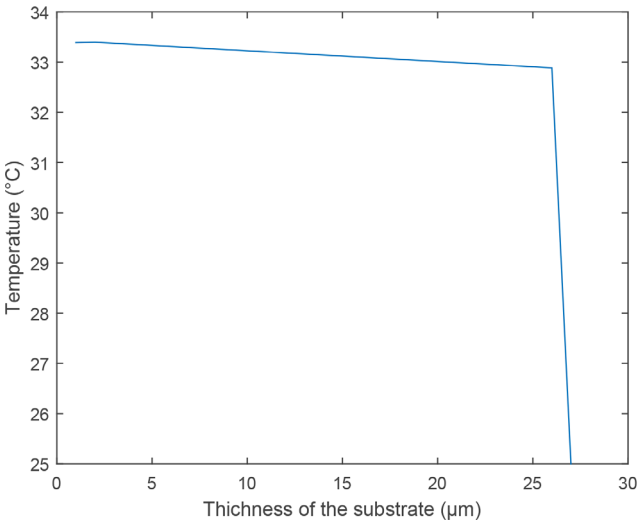

(c)

Fig. 17 Temperature distribution through the integrated inductor in the, (a) winding, (b) dielectric, (c) substrate

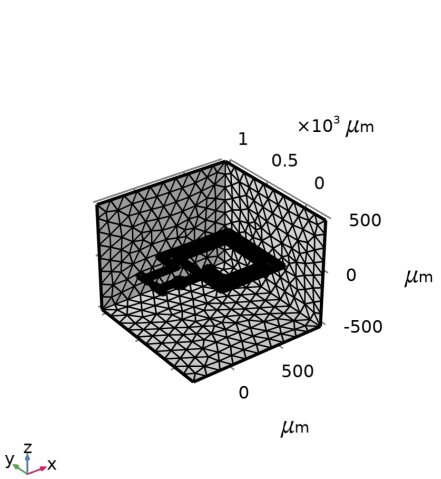

Fig. 18 Mesh in air core inductor

The temperature profile of winding is constant; it decreases in dielectric and substrate layers.

Using these results, it can be observed that for the thermal conduction problem with uniform heating, finite difference method can be used to investigate the temperature distribution inside the layer integrated inductor.

3.2 3D finite element method simulation

The planar integrated inductor, provided with the heat equation is solved by the 3D finite element method [30, 31]. The adopted mesh of the computation domain is refined as shown in Fig. 18.

Fig. 19 shows the temperature distribution in air core inductor. The temperature attained is from 53.3 °C. The heat source is transferred to the air by natural convection. This is because the winding increases the heat dissipation area in the proposed inductor. Fig. 20 shows the mesh in magnetic core inductor.

Fig. 21 shows the temperature distribution in magnetic core inductor. The temperature attained is from 33 °C. Losses due to air core inductor are much greater than losses due to magnetic core inductor. The loss is reduced, and the efficiency is improved effectively. The performance of this proposed magnetic core inductor is verified. Compared with conventional planar inductor, the proposed inductor has better thermal management, better thermal management reduces temperature rise, allowing the proposed inductor to carry higher currents. The required temperature value depends on the geometry of an underpass, magnetic core material thickness and properties.

As shown in Fig. 22, the temperature is pushed to the side of the conductor. This is because the magnetic core decreases the heat dissipation area in the component.

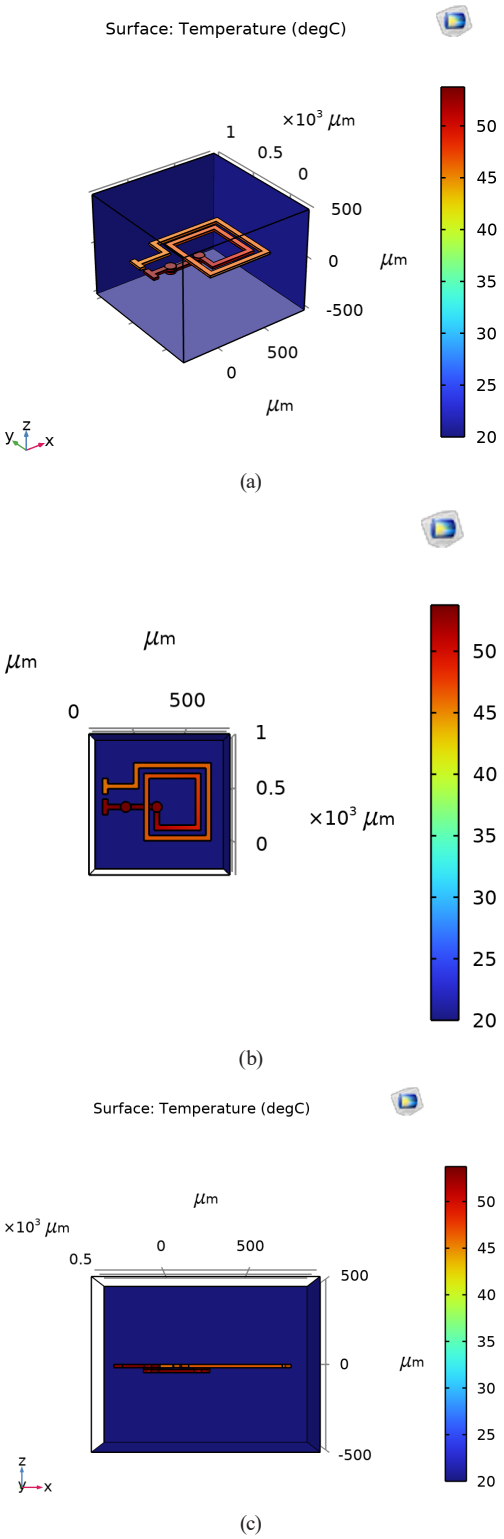

Fig. 19 Temperature distribution in air core inductor, (a) general view, (b) top view, (c) front view

4 Conclusion

In this article, the design process of a new integrated planar spiral inductor was described in detail, which is designed by the underpass with circular via. The element difference

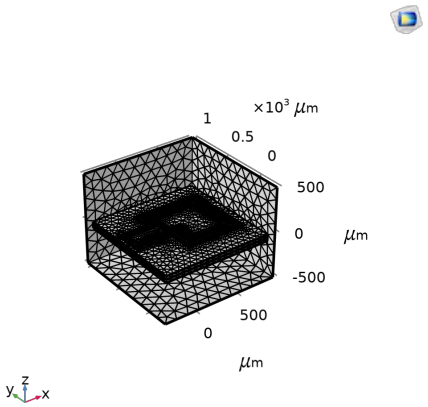

Fig. 20 Mesh in magnetic core inductor

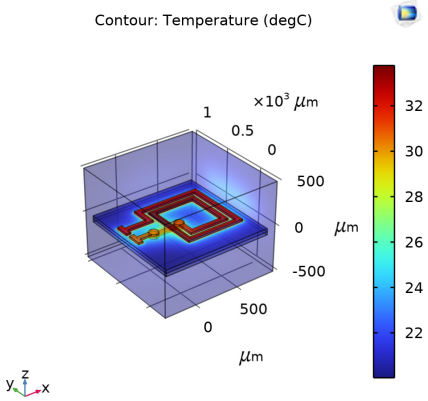

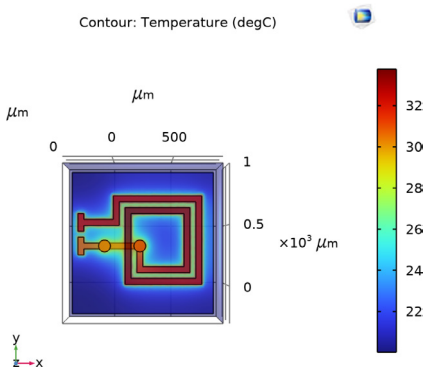

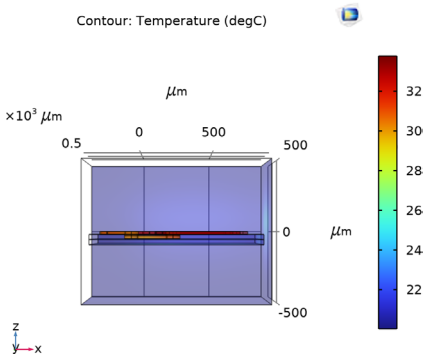

Fig. 21 Temperature distribution in magnetic core inductor, (a) general view, (b) top view, (c) front view

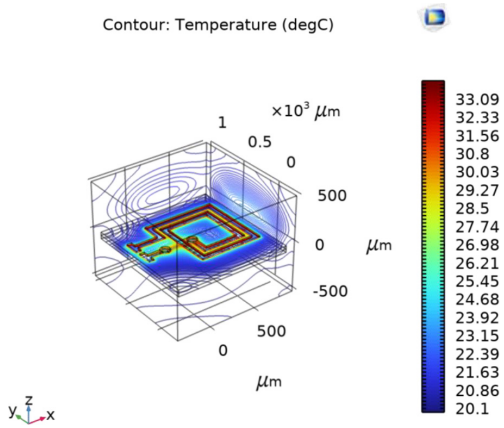

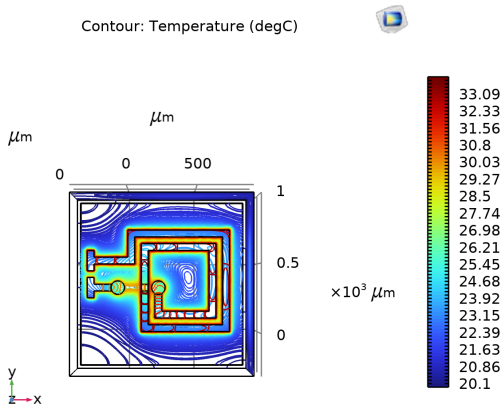

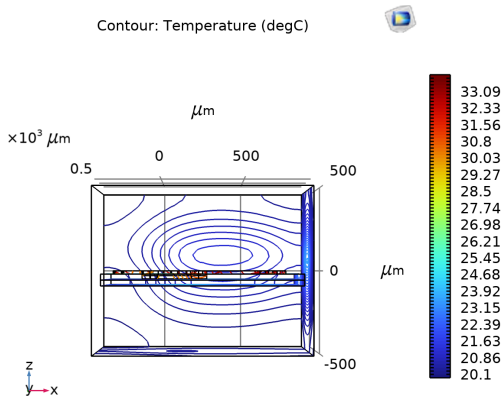

Fig. 22 Contour temperature distribution in magnetic core inductor, (a) general view, (b) top view, (c) front view

method is used to determine the temperature distribution in layers of different materials, given the source of heat generated and the properties of the layer materials. This model for a case has been compared with a 3D finite element method simulation using heat transfer module of the Comsol software [29]. A good correlation between analytical calculation using MATLAB software [31] and finite element method simulation tool [29] for the temperature distribution in the integrated planar spiral component has

been observed according to the assumptions made. It, also results the finite element software [29] is particularly suitable as a visualization tool for thermal behavior.

The result shows that the new design of an underpass and added layer magnetic core can enhancement inductance, quality factor, decrease losses and increase a temperature.

References

[1] Ding, Y., Fang, X., Wu, R., Guo, Q., Sin, J. K. O. "A Suspended Thick-Winding Inductor for Integrated Voltage Regulator Applications", IEEE Electron Device Letters, 41(1), pp. 95–98, 2020. https://doi.org/10.1109/LED.2019.2953554

[2] Barlik, R., Nowak, M., Grzejszczak, P., Zdanowski, M. "Estimation of power losses in a high-frequency planar transformer using a thermal camera", Archives of Electrical Engineering, 65(3), pp. 613–627, 2016. https://doi.org/10.1515/aee-2016-0044

[3] Górecki, K., Detka, K. "Influence of Power Losses in the Inductor Core on Characteristics of Selected DC–DC Converters", Energies, 12(10), 1991, 2019. https://doi.org/10.3390/en12101991

[4] Benhadda, Y., Hamid, A., Lebey, T., Allaoui, A., Derkaoui, M., Melati, R. "Thermal Behavior of an Integrated Square Spiral Micro Coil", Telkomnika: Indonesian Journal of Electrical Engineering, 14(2), pp. 250–265, 2015. https://doi.org/10.11591/telkomnika.v14i2.7361

[5] Yaya, D. D., Bechir, M. B., Youssouf, M. K., Soultan, M., Kahlouche, F., Capraro, S., Siblini, A., Chatelon, J. P., Rousseau, J. J. "Characterization of integrated inductors with one and two YIG layers for low-power converters (1 W)", EPJ Web of Conferences, 75, 06002, 2014. https://doi.org/10.1051/epjconf/20147506002

[6] Allaoui, A., Hamid, A., Spiteri, P., Bley, V., Lebey, T. "Thermal modeling of an integrated inductor in a micro-converter", Journal of Low Power Electronics, 11(1), pp. 63–73, 2015. https://doi.org/10.1166/jolpe.2015.1366

[7] Coulibaly, S., Ambroise, D. K., Georges, L. "Thermal Modeling of a Multilayer Integrated LC Filter for Temperature Distribution Calculation", Engineering, 11(11), pp. 759–767, 2019. https://doi.org/10.4236/eng.2019.1111050

[8] Detka, K., Górecki, K. "Influence of the Size and Shape of Magnetic Core on Thermal Parameters of the Inductor", Energies, 13(15), 3842, 2020. https://doi.org/10.3390/en13153842

[9] Derkaoui, M., Benhadda, Y., Hamid, A., Temmar, A. "Design and Modeling of Octagonal Planar Inductor and Transformer in Monolithic Technology for RF Systems", Journal of Electrical Engineering & Technology, 16(3), pp. 1481–1493, 2021. https://doi.org/10.1007/s42835-021-00692-x

[10] Melati, R., Hamid, A., Thierry, L., Derkaoui, M. "Design of a new electrical model of a ferromagnetic planar inductor for its integration in a micro-converter", Mathematical and Computer Modelling, 57(1–2), pp. 200–227, 2013. https://doi.org/10.1016/j.mcm.2011.06.014

[11] Namoune, A., Taleb, R., Mansour, N. "Simulation of an integrated spiral inductor and inter-digital capacitor in a buck micro converter", Journal for Control, Measurement, Electronics, Computing and Communications, 64(2), pp. 268–276, 2023. https://doi.org/10.1080/00051144.2022.2142572

[12] Li, S.-H. Hsu, S. S. H., Chen, K.-W., Lin, C.-S., Chen, S.-C., Zhang, J., Tzeng, P.-J. "Fully Symmetric 3-D Transformers with Through-Silicon via IPD Technology for RF Applications", IEEE Transactions on Components, Packaging and Manufacturing Technology, 9(11), pp. 2143–2151, 2019. https://doi.org/10.1109/TCPMT.2019.2943404

[13] Niknejad, A. M., Meyer, R. G. "Analysis, design, and optimization of spiral inductors and transformers for Si RF ICs", IEEE Journal of Solid-State Circuits, 33(10), pp. 1470–1481, 1998. https://doi.org/10.1109/4.720393

[14] Burghartz, J. N., Edelstein, D. C., Soyuer, M., Ainspan, H. A., Jenkins, K. A. "RF Circuit design aspects of spiral inductors on silicon", IEEE Journal of Solid-State Circuits, 33(12), pp. 2028–2034, 1998. https://doi.org/10.1109/4.735544

[15] Mohan, S. S., del Mar Hershenson, M., Boyd, S. P., Lee, T. H. "Simple Accurate Expressions for Planar Spiral Inductances", IEEE Journal of Solid-State Circuits, 34(10), pp. 1419–1424, 1999. https://doi.org/10.1109/4.792620

[16] Musunari, S., Chapman, P. L., Zou, J., Liu, C. "Design issues for monolithic DC-DC converters", IEEE Transactions on Power Electronics, 20(3), pp. 639–649, 2005. https://doi.org/10.1109/TPEL.2005.846527

[17] Bajwa, R., Yapici, M. K. "Integrated On-Chip Transformers: Recent Progress in the Design", Sensors, 19(16), 3535, 2019. https://doi.org/10.3390/s19163535

[18] Niknejad, A. M., Meyer, R. G. "Analysis of Eddy-Current Losses Over Conductive Substrates with Applications to Monolithic Inductors and Transformers", IEEE Transactions on Microwave Theory and Techniques, 49(1), pp. 166–176, 2001. https://doi.org/10.1109/22.900004

[19] Mohan, S. S., Yue, C. P., del Mar Hershenson, M., Wong, S. S., Lee, T. H. "Modeling and Characterization of On-Chip Transformers", In: International Electron Devices Meeting 1998. Technical Digest (Cat. No.98CH36217), San Francisco, CA, USA, 1998, pp. 531–534. ISBN 0-7803-4774-9 https://doi.org/10.1109/IEDM.1998.746414

[20] Valkodai, A., Manku, T. "Modeling and designing silicon thin-film inductors and transformers using HSPICE for RFIC applications", Integration, 24(2), pp. 159–171, 1997. https://doi.org/10.1016/S0167-9260(97)00031-X

[21] Long, J. R. "Monolithic Transformers for Silicon RF IC Design", IEEE Journal of Solid-State Circuits, 35(9), pp. 1368–1382, 2000. https://doi.org/10.1109/4.868049

[22] Mayevskiy, Y., Watson, A., Francis, P., Hwang, K., Weisshaar, A. "A New Compact Model for Monolithic Transformers in Silicon-Based RFICs", IEEE Microwave and Wireless Components Letters, 15(6), pp. 419–421, 2005. https://doi.org/10.1109/LMWC.2005.850558

[23] Hsu, H.-M., Tseng, C.-W., Chan, K.-Y. "Characterization of On-Chip Transformer Using Microwave Technique", IEEE Transactions on Electron Devices, 55(3), pp. 833–837, 2008. https://doi.org/10.1109/TED.2007.914841

[24] Hsu, H.-M., Tsai, M.-C. Huang, K.-H. "An on-chip transformer in silicon-based technology", Journal of Micromechanics and Microengineering, 17(8), 1504, 2007. https://doi.org/10.1088/0960-1317/17/8/012

[25] Jin, X., Xiao, X., Sun, Y., Pu, H., Peng, Y., Luo, J. "Monolithic transformer and its application in a high-speed optical interconnect VCSEL driver", Analog Integrated Circuits and Signal Processing, 99(3), pp. 645–654, 2019. https://doi.org/10.1007/s10470-018-01386-7

[26] Oumar, D. A., Boukhari, M. I., Taha, M. A., Capraro, S., Piétroy, D., Chatelon, J. P., Rousseau, J. J. "Characterization Method for Integrated Magnetic Devices at Lower Frequencies (up to 110 MHz)", Journal of Electronic Testing, 35(2), pp. 245–252, 2019. https://doi.org/10.1007/s10836-019-05790-3

[27] Davis, M. F., Sutono, A., Yoon, S.-W., Mandal, S., Bushyager, M., Lee, C.-H., Lim, K., Pinel, S., Maeng, M., Obatoyinbo, A., Chakraborty, S., Laskar, J., Tentzeris, E. M., Nonaka, T., Tummala, R. R. "Integrated RF architectures in fully-organic SOP technology", IEEE Transactions on Advanced Packaging, 25(2), pp. 136–142, 2002. https://doi.org/10.1109/TADVP.2002.803261

[28] Leite, B., Kerhervé, E., Bégueret, J.-B., Belot, D. "Substrate shielding of transformers in millimeter-wave integrated circuits", 73(1), pp. 209–215, 2012. https://doi.org/10.1007/s10470-011-9819-y

[29] COMSOL Multiphysics® "COMSOL Multiphysics®, (6.0)", [computer program] Available at: https://www.comsol.com/ [Accessed: 23 January 2021]

[30] Derkaoui, M., Benhadda, Y., Hamid, A. "Modeling and simulation of an integrated octagonal planar transformer for RF systems", SN Applied Sciences, 2(4), 656, 2020. https://doi.org/10.1007/s42452-020-2376-1

[31] Kharbouch, H., Guettaf, Y., Hamid, A., Bley, V., Benhadda, Y. "Design and Implementation of Inductors with Variable Conductor Width Integrated in a Boost Micro Converter", Transactions on Electrical and Electronic Materials, 22(4), pp. 519–530, 2021. https://doi.org/10.1007/s42341-020-00261-5

[32] MathWorks "Matlab, (2015a)", [computer program] Available at: https://www.mathworks.com [Accessed: 16 March 2021]